Topological characterization of neutron star crusts

C. O. Dorso and P. A. Giménez Molinelli

Departamento de Física, FCEN, Universidad de Buenos Aires, Núñez, Argentina

J. A. López

Department of Physics, University of Texas at El Paso, El Paso, Texas 79968, USA

Neutron star crusts are studied using a classical molecular dynamics model developed for heavy-ion reactions. After the model is shown to produce a plethora of the so-called pasta shapes, a series of techniques borrowed from nuclear physics, condensed matter physics, and topology is used to craft a method that can be used to characterize the shape of the pasta structures in an unequivocal way.

I. INTRODUCTION

Neutron stars created in the death of a massive star are composed of a dense core containing an excess of neutrons over protons, thus justifying the name. With a mass between 1 and 3 solar masses and a radius of about 10 km, the stars are topped with a crust of about a kilometer thick where the β-decay-produced neutrons form neutron-rich nuclear matter immersed in a sea of electrons. The crust density ranges from normal nuclear density ($\sim$3 × 10^{14} g/cm^3) at a depth of about 1 km, to the neutron drip density ($\sim$4 × 10^{11} g/cm^3) at about 1/2 km, to a light mix of neutron-rich nuclei with densities decreasing practically to zero in the neutron star envelope. Likewise the proton-to-nucleon ratio also varies from $\sim$0.25 to $\sim$0.5 through the crust [1], and the temperature from cold nuclear matter to about 1 MeV. The study of the structure of such crust is the purpose of the present work.

Studies of low-density nuclear matter have revealed that the attractive-repulsive interplay of nuclear and Coulomb forces drives low-density nuclear matter to form nonuniform structures which are collectively known as "nuclear pasta." Such arrangements go from condensed phases with voids filled with nuclear gas, to "lasagna-like" layers of nuclei surrounded by gas, to "spaghetti-like" rods embedded in a nuclear gas, to ever-decreasing "meatball-like" clumps which practically dissolve into a gaseous phase [2].

Early investigations have used static models which rely mostly on energy considerations to determine the structures that are most energetically favorable. Among the various theories proposed, the ones used most recurrently are the compressible liquid drop model [3–5], the extended Thomas-Fermi model [2,6–8], and the Hartree-Fock method [5,9–13].

On the other hand, there are dynamical models that go beyond mean fields to predict the formation of the pasta phases as an asymptotic equilibrium state resulting from an evolution of a dynamical system. The most used methods are semiclassical molecular dynamics [14–16] and quantum molecular dynamics [17–22].

On the general composition of the pasta, most models agree on the formation of varying structures at subnormal densities but not on how the sequence of phases arises. Since the physical mechanism responsible for the phase transition

pattern is a subtle interplay between Coulomb and nuclear energies, which vary only by a few keV/fm^3 between phases, the precise transition pattern is easily altered by the ingredients of the theoretical models. The fact that the Coulomb interaction between the electron sea and the nucleons—whose screening effect stabilizes the overall system, modifying its structure—must be treated under different approximations in different models [22] complicates any cross-model comparison even more.

An additional problem which makes comparisons among models difficult, or impossible in some cases, is the lack of a quantifiable characterization of different pasta phases. The identification of phases has been done mainly through visual inspections of snapshots of spatial nucleon distributions obtained from calculations [23]. The quantum molecular dynamics approach of Ref. [17], for example, produces nuclear holes, slabs, cylinders, and spheres similar to those predicted by the Thomas-Fermi model [2,6,7], but at different densities and temperatures.

In spite of this, the pasta phases have been characterized globally. For instance, static models have been used to calculate average densities [8] and volume fractions of the different phases [24]. Pasta bulk properties, such as the shear viscosity [25] and diffusion coefficients [26], have also been obtained using molecular dynamics simulations. Refined studies have used radial correlation functions to characterize the nucleon distributions [19] and the pasta structure factor to study charge density fluctuations [27].

More recently, shape characterizations were attempted both in dynamical simulations and with static models; the former use topological measures such as the Minkowski functionals and the Euler characteristics [23], while the latter modified the liquid drop model with a curvature correction to detect structure shape changes [28].

Thus we have the motivation of the present study: How do we achieve a precise enough characterization of the pasta phases? What property can be used to signal a change of pasta phase? The purpose of the present work is to construct the instruments needed to properly quantify the pasta structures.

By taking advantage of the microscopic details produced by a classical molecular dynamics model, this investigation

combines the power of cluster-detection algorithms used in nuclear collisions with indicators borrowed from condensed matter physics and topology to detect the transitions between pasta phase structures in a quantitative way.

After an introduction of the model, we will introduce a series of techniques used to classify the pasta structures that will help us reach our goal. Starting from global measures to understand the cluster composition (fragment size distribution, nucleon mobility and persistence, fragment isotopic composition, and radial distribution function), we will progress into topological tools (Minkowski functionals) that will allow us to characterize the shape of the pasta structures as well as to detect changes between them. A final discussion of the results will then help us reach a series of conclusions and to draw an outlook for future tasks.

II. NUCLEON DYNAMICS

To study the structure of stellar crusts it is necessary understand the behavior of nucleons at the proper densities, temperatures, and proton-to-neutron ratios; such knowledge comes from the study of heavy-ion fragmentations. The initial statistical studies of nuclear collisions of the 1980s [29,30] rapidly gave way to dynamical theories based on classical, semiclassical, and quantum approaches.

The semiclassical models use the Boltzmann-Uehling-Uhlenbeck equations [31] to track the time evolution in phase space of the probability of finding a particle moving in a mean field. On the other hand, the quantum molecular dynamics models (QMD) solve the equations of motion of nucleon wave packets moving within mean fields. Unfortunately, these theories either do not lead to cluster formation or yield a poor description of cluster properties and both must resort to the use of all sorts of extraneous techniques such as adding fragments by hand, coupling to "afterburners" to produce secondary decays [32], and introducing hidden adjustable parameters (e.g., width of wave packets, number of test particles, and modifications of mean fields, effective masses, and cross sections, etc.) to satisfy the operator's taste.

These problems are either nonexistent or much reduced in classical models. Classical dynamical models generally solve Newton's equations of motion to track individual nucleons moving under two-body potentials; coupled to cluster-recognition algorithms these calculations yield microscopic views of nuclear reactions as well as of nuclear structures. The only apparent disadvantage of the classical models would be the lack of quantum effects, such as Pauli blocking; fortunately, in stellar environments the very small nucleon energies lead to frozen-like structures where the blocking of momentum-transferring collisions ceases to be relevant. [See Ref. [33] for a calculation of the mean thermal wavelength of a nucleus in stellar conditions to justify the use of a classical approach.]

Let this rather long preamble serve to justify extending the use of a classical model designed for nuclear reactions to the study neutron star crusts. In this work we use a classical model to obtain a detailed microscopic picture of the pasta structures and be able to detect transitions between phases.

A. Classical molecular dynamics

We use a molecular dynamics code combined with algorithms for cluster recognition. Our classical molecular dynamics model, CMD [34], is based on the pioneering work of Pandharipande [35] and has been very fruitful in nuclear studies of, among other phenomena, neck fragmentation [36], phase transitions [37,38], critical phenomena [39,40], the caloric curve [41,42], and isoscaling [43,44] all without any adjustable parameters. Readers are directed to these references for further details on the model; here only a brief synopsis will be presented along with its extension to infinite systems.

In a nutshell, CMD treats nucleons as classical particles interacting through a two-body potential and solves the coupled equations of motion of the many-body system to obtain the time evolution of all particles. Since the $(\mathbf{r}, \mathbf{p})$ information is known for all particles at all times, it is possible to know the structure of the nuclear medium from a microscopic point of view.

CMD uses the phenomenological potentials developed by Pandharipande [35]:

$$V_{np}(r) = V_r[\exp(-\mu_r r)/r - \exp(-\mu_r r_c)/r_c]$$
$$- V_a[\exp(-\mu_a r)/r - \exp(-\mu_a r_a)/r_a]$$
$$V_{NN}(r) = V_0[\exp(-\mu_0 r)/r - \exp(-\mu_0 r_c)/r_c],$$

where V_{np} is the potential between a neutron and a proton and it is attractive at large distances and repulsive at small ones, and V_{NN} is the interaction between identical nucleons and it is purely repulsive. Notice that no bound state of identical nucleons can exist; also notice that, in contrast to potentials used by other models [15], these potentials have a hard core.

The cutoff radius is $r_c = 5.4$ fm, after which the potentials are set to zero. Two sets of values for the Yukawa parameters μ_r, μ_a, and μ_0 were fixed by Pandariphande to correspond to infinite-nuclear-matter systems with an equilibrium density of $\rho_0 = 0.16$ fm^{-3}, a binding energy $E(\rho_0) = 16$ MeV/nucleon, and compressibility of about 250 MeV ('medium') or 535 MeV ('stiff') [35]. In the past, a combination of Monte Carlo and molecular dynamics techniques was applied within a statistical formalism to obtain neutron star crust properties [15].

B. Simulating the neutron star crust

To study the neutron star crust we use CMD to simulate an infinite medium. Systems with 2000 or 3000 nucleons were constructed and replicated with periodic boundary conditions in 26 surrounding cells. In particular, the proton ratios used were $x = Z/A = 0.5$ (1000 neutrons and 1000 protons) or 0.3 (2000 neutrons and 1000 protons). The cubical box size used was adjusted as to achieve densities between $\rho = 0.01$ fm^{-3} (about $\rho_0/15$) and ρ_0.

As the crust is expected to be embedded in a degenerate electron gas produced by weak decays during the supernova explosion, it is necessary to take into account its Coulomb interaction. Although the nucleon-electron system is overall neutral and β-equilibrated, the infinite Coulomb range requires the use of some approximation; two common approaches are

the Thomas-Fermi screened Coulomb potential (used in QMD in [17]) or the Ewald summation procedure [45]. Although CMD is able to operate under either approximation, in this work the former is adopted (and see [46] for a comparison of methods under CMD).

By approximating the electron gas as a uniform ideal Fermi gas at the same number density as the protons, its effect can be included in the nucleon's equations of motion by means of the screened Coulomb potential obtained from the Poisson equation:

$$V_C^{(Scr)}(r) = \frac{e^2}{r} \exp(-r/\lambda),$$

where the relativistic Thomas-Fermi screening length is $\lambda = (\pi^2/2e)[k_F^2(k_F^2 + m_e^2)]^{-\frac{1}{4}}$, m_e is the electron mass, $k_F = (3\pi^2\rho_e)^{1/3}$ is the electron Fermi momentum, and ρ_e is the electron gas number density equal to that of the protons. The size of the simulation cell, $L = (A/\rho)^{1/3}$, should be significantly larger than λ; in our case we satisfy such a requirement by using the prescription of [15] and setting $\lambda = 10$ fm.

The trajectories of individual nucleons, now governed by the Pandharipande and the screened Coulomb potentials, are then tracked using a Verlet algorithm with energy conservation of $O(0.01\%)$. The system is force-heated or cooled using isothermal molecular dynamics with the Andersen thermostat procedure [47], which gradually cools in small temperature steps while reaching thermal equilibrium at every step. We focus on the range of $T = 0.1$ to 1.0 MeV; although this last temperature is large for stellar crusts, in terms of the nucleon dynamics it practically corresponds to a frozen state.

III. CHARACTERIZING THE CRUST

In contrast to most QMD simulations, which tend to track individual evolutions, here we obtain reliable statistics by sampling 200 times each configuration with specific x, ρ, and T conditions. Figure 1 shows a smörgåsboard of Italian delicacies produced by CMD with $x = 0.5$, $T = 0.1$ MeV and twenty different densities; notice that for clarity the figures do not show single nucleons, i.e., the gaseous phase. In spite of their beauty, one cannot use those figures to properly characterize the pasta shapes; for that one must resort to other, less visually attractive, techniques.

On each of the configurations achieved, the nucleon (**r**, **p**) information is recorded and used later to identify clusters and to characterize the structure by means of the liquid structure function and the Minkowski functionals.

A. Cluster composition

The nucleon positions are used to identify clusters by means of the minimum spanning tree (MST) algorithm refined for nucleon dynamics in [48,49]. In summary, MST looks for correlations in configuration space: a particle i belongs to a cluster C if there is another particle j that belongs to C and $|\mathbf{r}_i - \mathbf{r}_j| \leqslant r_{cl}$, where r_{cl} is a clusterization radius, which is set to 3.0 fm. In spite of using only r-space correlations,
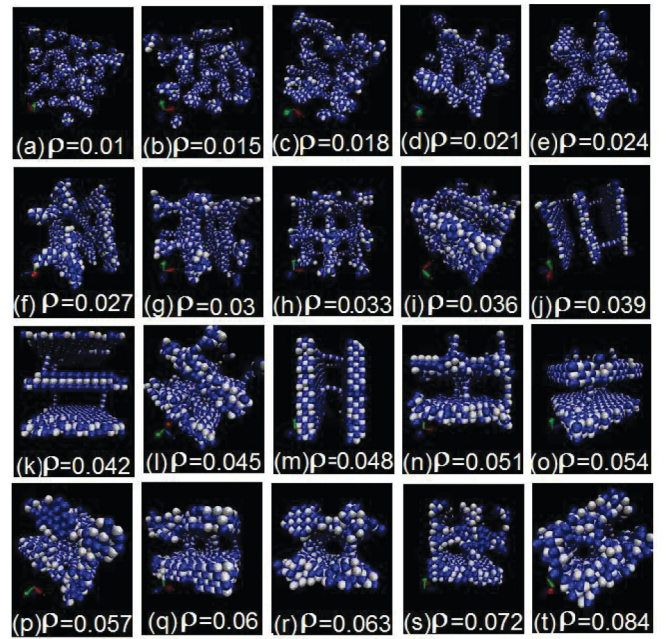

FIG. 1. (Color online) Smörgåsboard of pasta shapes corresponding to the densities shown and to $x = 0.5$ and $T = 0.1$ MeV.

MST yields accurate results in the case of stellar crusts due to the low temperatures and small momentum transfer, and thus here it is preferred over other more robust cluster-detection algorithms (such as the early cluster recognition algorithm, ECRA [50], which take into account relative momenta and binding energies). In our case of periodic boundary conditions, the MST method was modified to recognize fragments that extend into adjacent cells.

Figure 2 shows examples of the fragment population obtained with CMD-MST at $x = 0.3$, $\rho = 0.015$ fm^{-3}, and four different temperatures; of particular interest is the evolution of the clustering as a function of the temperature as it shows a trend opposite to that observed in nuclear collisions. The figure
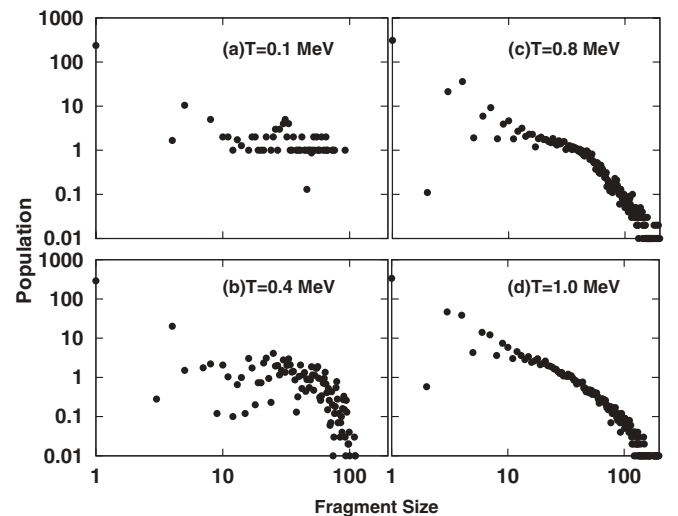

FIG. 2. Temperature evolution of the fragment size distribution obtained from 200 configurations with $x = 0.3$ and $\rho \approx \rho_0/10$.
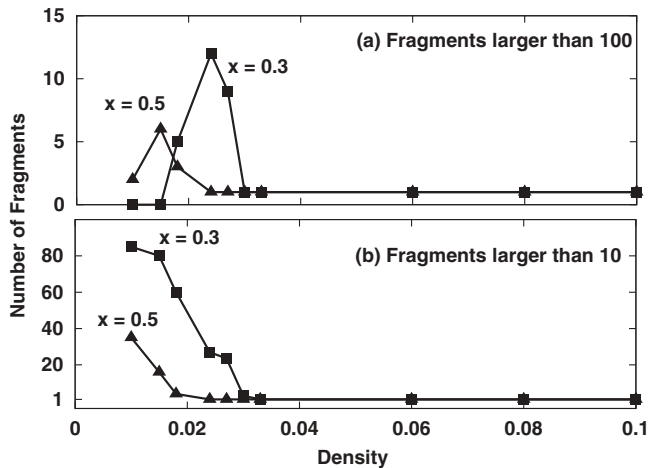
FIG. 3. Relative abundance of large clusters as a function of density for $x = 0.3$ and 0.5 at $T = 0.1$ MeV.

shows a typical evolution for the range $0.1 < T < 0.1$ MeV and, as can be clearly observed, the large fragment multiplicity increases with T. This is ithe opposite to what happens in heavy-ion reactions at high energies where heavier fragments shrink in size by particle evaporation during the final expansion stage of the reaction. In the case of infinite systems, however, the lack of expansion (and lack of a reduced pressure) makes evaporation less probable and, combined with the possibility of connecting fragments to neighboring cells, it favors the growth of cluster sizes as soon as the nucleons reach enough mobility with increasing T.

The growth of large-fragment multiplicity can also be seen as a function of the density. Figure 3 shows a typical behavior of the relative multiplicity of large clusters, $A > 100$ and $A > 10$, obtained at different densities for both $x = 0.3$ and 0.5 at $T = 0.1$ MeV. As the density increases, the number of clusters of $A > 100$ increases practically linearly with ρ up until a single large fragment is formed; smaller clusters of $A > 10$ are abundant at low densities but decrease for larger densities. The density at which the number of large clusters condense into a single one can be thought of as a "percolation" density; this value, of course, depends on the simulation parameters such as number of particles, cell size, temperature, etc.; for the cases shown, the percolation densities are $\rho \approx 0.03$ fm^{-3} for $x = 0.3$ and $\rho \approx 0.024$ fm^{-3} for $x = 0.5$ at $T = 0.1$ MeV.

The dynamics of the nucleons within systems in equilibrium can be gauged through their average displacement as a function of time, i.e., through the time steps of the simulation. Figure 4 shows the root-mean-square displacement of the nucleons from their original position in 200 time steps; as a metric one must remember that the range of the potential is 5.4 fm and (as we will see in Sec. III B) the interparticle distance at these densities is of the order of 1.7 fm. The increment in mobility as a function of the temperature is obvious.

Likewise, the microscopic stability of the clusters can be quantified through the "persistency" [51,52], which measures the tendency of members of a given cluster to remain in the same cluster. Figure 5 shows the time evolution of the persistency for systems with $\rho = 0.015$ fm^{-3} and $x = 0.3$ at the listed temperatures; notice that a persistency of ~ 1
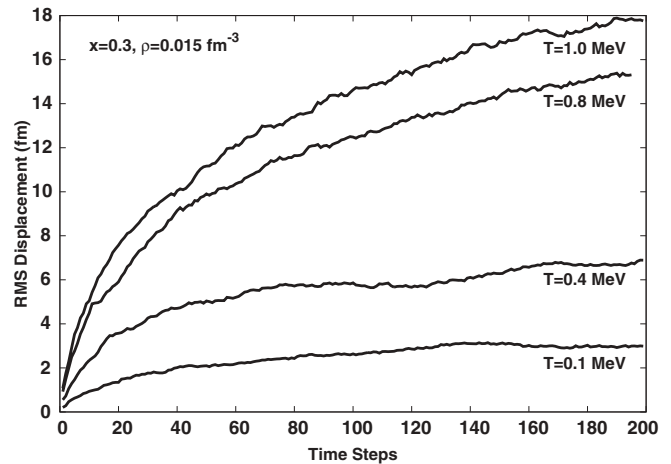

FIG. 4. Root-mean-square displacement of the nucleons from their original position as a function of the simulation time steps for systems with $\rho = 0.015$ fm^{-3} and $x = 0.3$ at the listed temperatures.

indicates that most of the particles remain in the same cluster, while smaller values indicate a larger exchange rate. The anticorrelation between this and the previous figure is clear: more mobility implies less persistency, and vice versa.

Another interesting descriptor is the isospin content of the clusters produced. By keeping track of the number of protons and neutrons on each fragment it is possible to determine the x value for each cluster. An example of this is shown in Fig. 6, where the x content of the fragments is plotted as a function of the mass of the clusters obtained at a density of $\rho = 0.015$ fm^{-3} and with $x = 0.5$ (top two plots) and $x = 0.3$ (bottom four). Several effects are noticeable: small clusters ($A \lesssim 10$) tend to have fewer protons than the average, resulting in smaller x values; for the case of $x = 0.3$ there is a prominent binding of one proton to two neutrons, which results in clusters of all sizes with values of $x \approx 1/3$; the previous effect is not present in the case of $x = 0.5$, in which all the clusters maintain their x values around $1/2$.
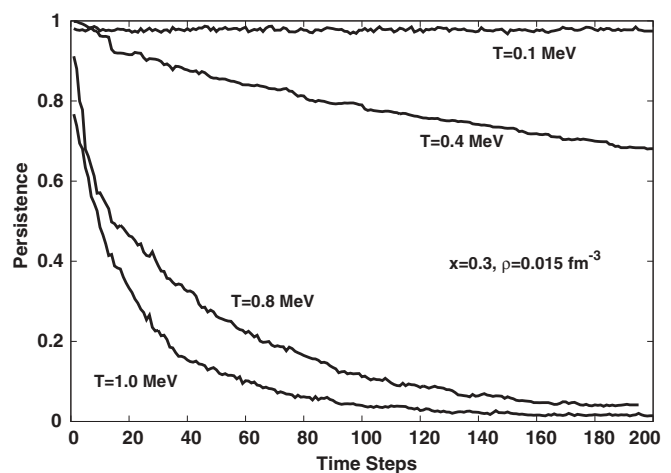

FIG. 5. Time evolution of the persistency for the listed temperatures as a function of the simulation time steps for $x = 0.3$ and $\rho = 0.015$ fm^{-3}.
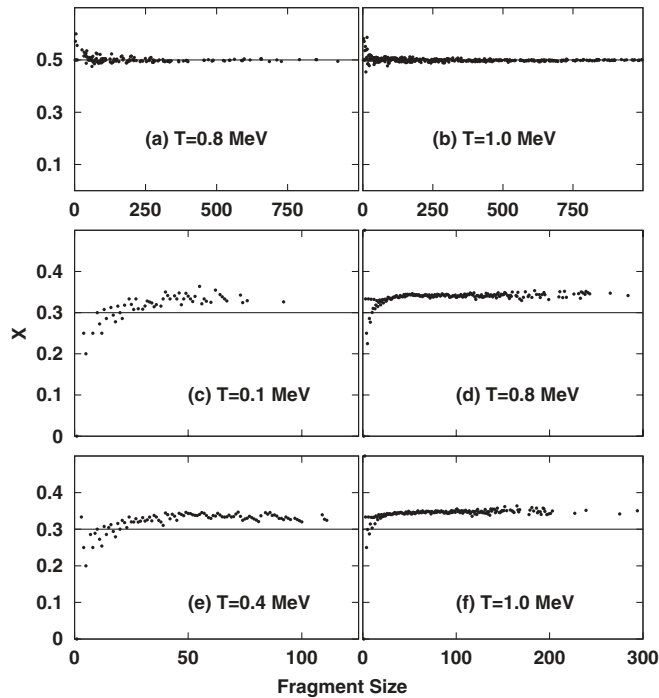
FIG. 6. Example of the x value ($x = p/A$) of the clusters vs their size, corresponding to systems with $\rho = 0.015$ fm^{-3} and $x = 0.5$ (top two plots) and $x = 0.3$ (bottom four plots) at the temperatures listed.

We close this section noticing that, in spite of being a good indicator of the percolating density, the cluster multiplicity is a poor descriptor of the pasta shapes. Stepping up in complexity, we now turn to the radial correlation function to probe the pasta *al dente*.

B. Pair correlation function

Another global characterization of the structure of nuclear matter is obtained from the pair correlation function, $g(r)$, which is the ratio of the average local density to the global density, $g(r) = \rho(r)/\rho_0$; it gives information about the spatial ordering of the nuclear medium.

For computing purposes, the pair correlation function $g(r)$ is taken as the conditional probability density of finding a particle at $\mathbf{r}_i + \mathbf{r}$ given that there is one particle at $\mathbf{r}_i$. Formally,

$$g(r) = \frac{V}{4\pi r^2 N^2} \left\langle \sum_{i \neq j} \delta(r - r_{ij}) \right\rangle,$$

where r_{ij} is $|\mathbf{r}_i - \mathbf{r}_j|$. For our case, this was calculated by constructing histograms of the distances between particles for several configurations obtained with the same x, ρ, and T and then averaging them; to include all particles and their images the range was extended to $r_{ij} \leqslant 1.5L$.

Figure 7 shows examples of $g(r)$ obtained for cases with 2000 nucleons, $x = 0.5$, $T = 0.1$ MeV, and densities $0.01 < \rho < 0.039$ fm^{-3}. The inset shows the case $\rho = 0.048$ fm^{-3} when the nearest neighbors are just as probable as second nearest neighbors, signaling the onset of a lasagna-type structure (cf. Fig. 1).
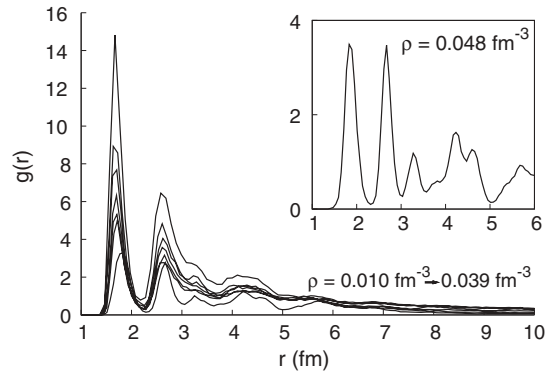

FIG. 7. Examples of the radial correlation function for $x = 0.5$, $T = 0.1$ MeV, and various densities. Also shown is the case when nearest neighbors are as probable as second nearest neighbors indicating a lasagna-type structure; r is in femtometers.

It is worth noticing that, in the case shown, the location of the nearest neighbors remains constant at $r \sim 1.7$ fm at all densities. This is because the position of the peak of $g(r)$ is an average between the location of neighbors in the gas-liquid mixture (since at subcritical densities the medium is metastable or unstable, it breaks into a gaseous and a condensed phase); the condensed matter at normal density has nearest neighbors at $r \approx 1.4$ fm [35].

Once again, in spite of the rich information derived from $g(r)$, it is still insufficient to tag the phases unequivocally; for this, other more complex constructs must be borrowed from cosmology and, ultimately, from topology.

C. Topological constructs

The most obvious properties of closed surfaces that can be used to characterize their shapes are the volume V, the surface area A, and the curvature. The latter is less trivial than the other two as it does not hold a unique value for a given shape but varies from point to point; however, mean curvatures of a closed body can be obtained by averaging procedures such as the "integral mean curvature," defined as $H = \int df (R_1 + R_2)/2R_1 R_2$, where R_1 and R_2 are the principal radii of curvature of the surface and df is a differential of area.
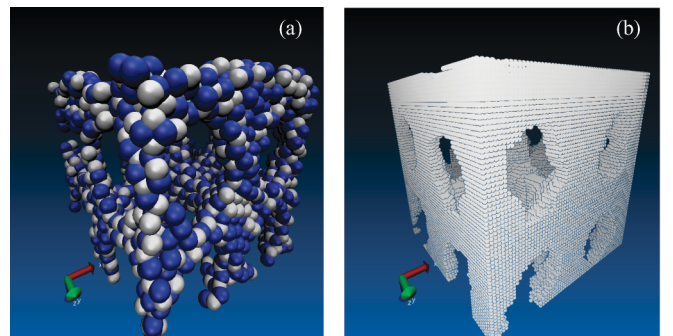

FIG. 8. (Color online) Sample transformation of a nuclear structure to a corresponding polyhedron. The structure corresponds to a case with $x = 0.5$, $\rho = 0.33$ fm^{-3}, and $T = 0.1$ MeV.
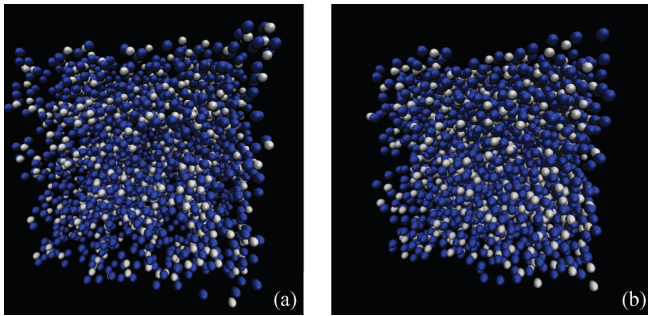
FIG. 9. (Color online) Spatial configurations formed under $T = 0.4$ MeV and $\rho = 0.045$ fm^{-3} (left) and $T = 1.0$ MeV and $\rho = 0.072$ fm^{-3} (right), both for $x = 0.3$.

In general, V, A, H, plus an interesting construct known as the Euler characteristic are collectively known as the "Minkowski functionals"; according to integral geometry the morphological properties of three-dimensional objects can be completely described in terms of them.

The XVIII-century work of Euler-L'Huilier showed that, independent of the shape of any polyhedra, deducting the number of edges from the number of vertices and adding
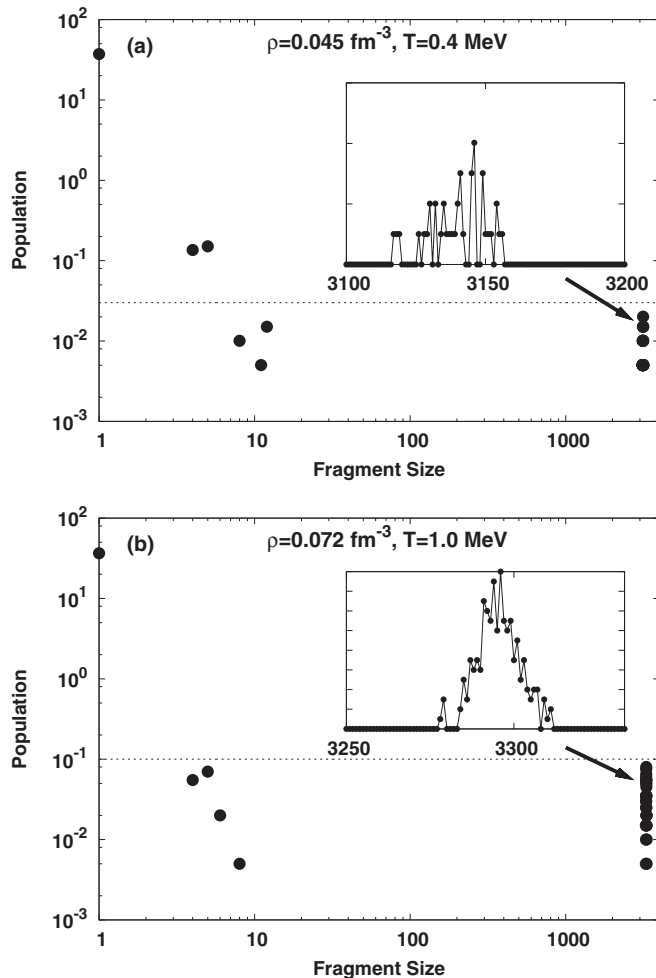

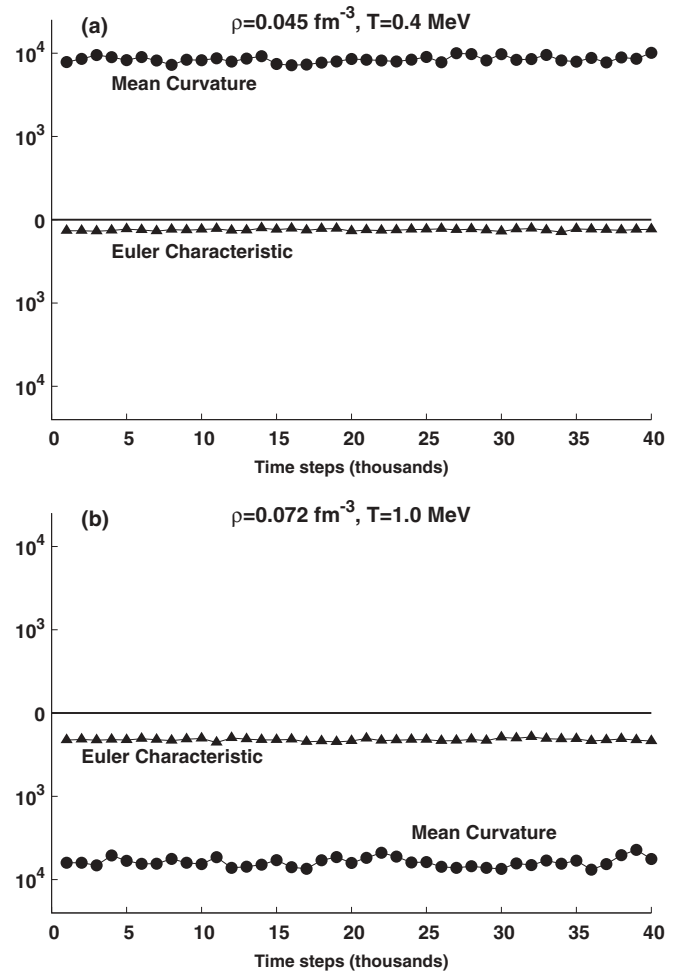FIG. 10. Multiplicites corresponding to Fig. 9; although not identical they are very similar.

FIG. 11. Euler and curvature of the structures shown in Fig. 9; the difference between the two cases is easy to spot.

the number of faces always yields 2 plus twice the number of cavities, a quantity now known as the Euler characteristic, χ. Although this previous property is for solids bounded by plane surfaces, it also applies in any three-dimensional surface with χ related to the total curvature of the surface through the Gauss-Bonnet theorem.

In topological terms, two orientable closed surfaces are homeomorphic to each other if their Euler characteristics are the same. Conversely, two homomeorphic closed surfaces will always have the same value of χ. Therefore, since our pasta niblets are all orientable, their Euler characteristic completely classifies them up to an homeomorphism; adding the rest of the Minkowski functionals eliminates such redundancy and guarantees a complete classification of the pasta shapes.

An immediate problem is the fact that the nuclear clusters are not polyhedra and do not even form closed surfaces. This obstacle, however, can be circumvented by replacing the nuclear structure with a scaffold-like armature composed of cells, each of which encloses one nucleon. In our case this is done through the algorithm of Michielsen and De Raedt [53], which has already been used in the study of stellar crusts, albeit in a different methodology [21].
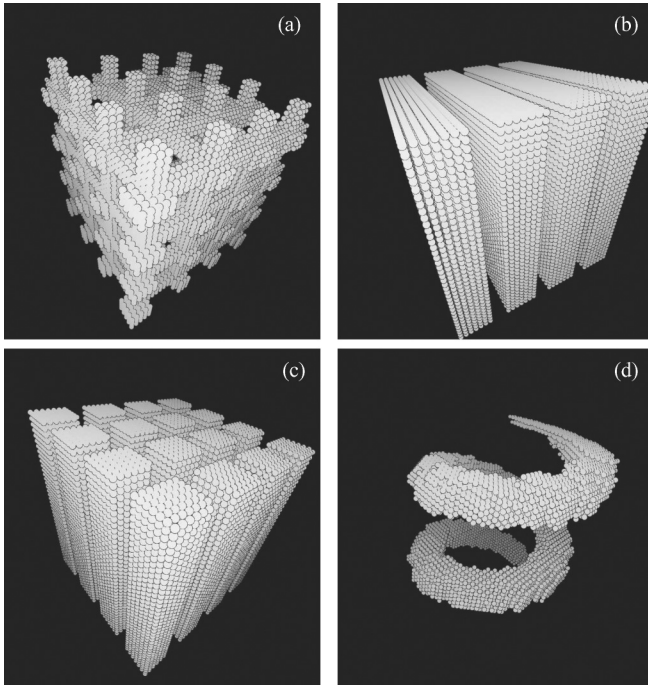
FIG. 12. Typical artificial "pastas" used to test the classification powers of the Euler-curvature combination. Respectively, they are the "jungle gym" (top left), "lasagnas" (top right), "straight spaghettis" (bottom left), and a "curled spaghetti."

FIG. 13. (Color online) Systematic classification of the artificial structures in terms of the curvature and Euler number.

Synoptically, the simulation volume is subdivided into a mall of cubic cells. Those cells which contain the coordinates of a nucleon are kept while the rest are deleted. The sizes of the cells are made smaller than the nearest neighbor distance found in $g(r)$ to enforce a one-particle-per-cell occupation, but not too small as to avoid creating spurious cavities between neighboring nucleons. It is on this imaginary platform that the Minkowski functionals of the nuclear structure are computed.

In general, χ equals the number of regions of connected grid cells minus the number of completely enclosed regions of empty grid cells. Two grid cells are connected if they are immediate neighbors, are next-nearest neighbors, or are connected by a chain of occupied grid cells. By characterizing the connected structure by its number of occupied cubes, n_c, edges, n_e, faces, n_f, and vertices, n_v, including possible contributions from the interior of the structure, the Minkowski functionals can be calculated through [53]

$$V = n_c, \quad A = -6n_c + 2n_f,$$
$$2B = 3n_c - 2n_f + n_c, \quad \chi = -n_c + n_f - n_e + n_v,$$

where V stands for the volume, A for the area, B for the mean breadth, and χ for the Euler number; the mean breadth measures the average "size" of a body and it is related to the integral mean curvature H mentioned before. Figure 8 shows a typical nuclear structure along with the grid constructed around it; the values of the Minkowski functionals obtained from such grid are curvature = 215 and Euler = −17; as we will see next such a shape can be classified as a "jungle gym."
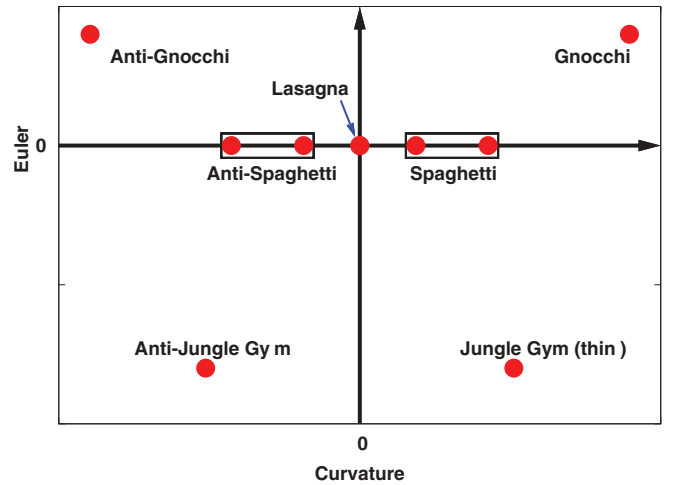
D. Topological classification of the pasta

To illustrate the use of topology to classify the pasta shapes let us use two seemingly similar structures obtained with $x = 0.3$ but at different densities and temperatures, namely, $\rho = 0.045$ fm^{-3} and $T = 0.4$ MeV and $\rho = 0.072$ fm^{-3} and $T = 1.0$ MeV. The spatial configurations of these two cases, practically identical to the eye, are presented in Fig. 9. Although there are minor differences (see insets), Fig. 10 shows that both configurations have very similar mass multiplicities.

The difference between the configurations, however, arises when we calculate the corresponding curvature and Euler numbers. Figure 11 shows the evolution of the curvature and of the Euler number as the simulation advances after equilibration. Clearly shown are the inverted values of Euler and the curvature for the two cases; while the curvature is positive (with fewer cavities than bellies) and large in the low-T, low-ρ case, it becomes negative (with more internal cavities than tummies) and smaller in the opposite case.

To investigate this point further, we created artificial structures in the form of gnocchi, spaghetti, lasagna, and crossed-lasagnas, which we call "jungle gym," and their inverse structures (with voids replacing particles and vice versa) and calculated the values of the two topological variables; some of the structures used are shown in Fig. 12 and their locations in the curvature-Euler plane are shown in Fig. 13. The magnitudes shown are determined by the size of the structure as well as the digitization cell size. In general one can conclude that lasagnas tend to lie near the origin, spaghettis have near-zero Euler numbers and positive curvatures, gnocchis have positive curvatures and Euler numbers, and jungle gyms have positive Euler number and negative curvature; all antistructures reverse the curvature but maintain the Euler characteristic. All cases calculated at all x values, densities, and temperatures were observed to satisfy this classification.

For instance, the structure in Fig. 8 with curvature 215 and Euler number −17 is clearly a jungle gym. Likewise, the structure in the left panel of Fig. 9, with both negative curvature and Euler number, can be classified as an "anti–jungle gym," whereas the accompanying structure with positive curvature

TABLE I. Classification of structures.

Density	$x = 0.5$			$x = 0.3$		
(fm^{-3})	Curvature	Euler	Topology	Curvature	Euler	Topology
0.01	(a) 100	100	G	(A) 96	27	G
0.015	73	50	G	92	7	G-S
0.018	58	17	G-S	79	−9	S
0.021	36	−25	S-J			
0.024	22	−28	S-J	58	−18	J-S
0.026				51	−39	J
0.027	9	−42	J-L	47	−37	J
0.03	10	−39	J-L	48	−7	S
0.033	9	−47	J	18	−75	J
0.036	8	−42	J			
0.039	−11	−6	L-AJ			
0.042	−15	−8	L-AJ			
0.045	1	−33	L-J	−54	−100	AJ
0.048	−5	−11	L			
0.051	−7	−17	AS-AJ	−94	−41	AJ
0.054	−1	−11	L-AJ			
0.057	−9	−30	AJ			
0.06	−9	−17	AJ	−100	66	AG
0.063	−10	−30	AJ			
0.072	−12	−8	AS-AJ	(L) −60	90	AG
0.084	(t) −19	−8	AJ			

and negative Euler number would have to be classified as a jungle gym.

Table I shows the classification of several of the structures obtained in our study at $T = 0.1$ MeV and at the listed densities, and Fig. 14 shows their location in the curvature-Euler plane; the $x = 0.5$ column of the table and the circular dots on the figure correspond to the structures presented in Fig. 1. As the absolute magnitude of the curvature and Euler number depends on the overall size of the structure, i.e., on the number of particles used, the data in Table I were normalized to have maximum absolute values of 100. In the table, the classifications are abbreviated as G for gnocchi, J for jungle
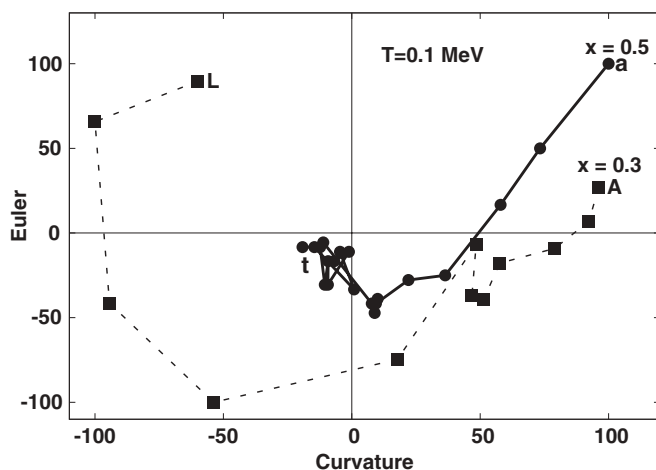
gym, L for lasagna, S for spaghetti, and AG, AJ, AL, and AS for the reverse structures.

IV. CONCLUDING REMARKS

And thus we have reached our objective. The combination of curvature and Euler number and a proper recognition of fragments appears to be robust enough to uniquely classify the shapes attained by the nucleons at densities, temperatures, and isospin content of interest in the study of neutron star crusts. In obtaining this result, classical molecular dynamics methods and associated tools (cluster-recognition algorithms, persistence, etc.) proved to be valuable, and we are now exploiting these in on-going investigations.

Comparing our approach to a previous application of the Minkowski functionals within a QMD model [21], we see the obvious methodological differences, such as the interaction potentials used, the treatment of the Coulomb interaction, etc., but we also identify one main advantage of our approach. While to calculate the Minkowski functionals QMD has to rely on proton and neutron density distribution functions constructed from the trial wave functions and with the use of extraneous parameters such as cutoff density values, CMD simply uses the particle positions to directly apply the Michielsen and De Raedt method [53] and evaluate the curvature and Euler numbers; the lack of fudging factors undoubtedly makes the CMD results more robust for topological classification purposes.

As hinted in [44], the role of the long-range Coulomb interaction has not been fully explored; current exploratory runs are indicating that the Coulomb interaction merely shifts the space scales a bit but is not an "if-and-only-if" requirement for the formation of clusters. In a parallel investigation [54] we have applied the CMD model and the topological methodology developed here to perform an in-depth study of the origin of clustering.

Along the same lines, given that the existence of the pasta phases depends exquisitely on the interplay between surface and Coulomb energy, it is critical to test the results obtained here using different potentials with varying ranges, strengths, and nuclear compressibility. In an on-going study [55] we plan to investigate this using two other potentials with medium and stiff compressibility and different interaction ranges.

Finally, and as part of our long-term research plan, we intend to connect our potential-based microscopic model to a macroscopic equation of state (EoS). Since CMD is applicable to any type of nuclear dynamics (collisions, hydrodynamic flow, etc.) while the EoS can only describe systems under thermal and chemical equilibrium, it is difficult at best to link the results obtained through CMD to the different terms of an EoS. Although macroscopic objects such as volume, surface, curvature, and symmetry energies are intrinsically linked to the properties of the interacting potentials, in the absence of a complete many-body theory their connection to the particle-particle interactions can only be obtained from averaging the microscopic results to obtain the macroscopic variables. In a future study this connection will be estimated for a variety of conditions including the nebulous transition from the cold

FIG. 14. Curvature-Euler coordinates of the structures listed in Table I. Labels "A," "a," "L," and "t" correspond, respectively, to the initial and final points in the table.

nuclear pasta shapes to the gas-liquid mixtures that occurs at higher temperatures and subsaturation densities.

Beyond our immediate scope is the possible connection that the Minkowski functionals can have with physical properties of the nuclear systems. Studies such as Ref. [56] have managed to link, e.g., curvature energies, scattering and diffusion properties (through spectral densities), order parameters, structure functions, correlation functions, critical points, and percolation thresholds with the various Minkowski functionals. Here we invite capable researchers to investigate these intriguing connections in future studies.

[1] P. Haensel and J. L. Zdunik, Astron. Astrophys. **229**, 117 (1990).

[2] K. Oyamatsu, Nucl. Phys. A **561**, 431 (1993).

[3] G. Baym, H. A. Bethe, and C. Pethick, Nucl. Phys. A **175**, 225 (1971).

[4] C. P. Lorenz, Ph.D. thesis, University of Illinois, 1991.

[5] F. Douchin and P. Haensel, Phys. Lett. B **485**, 107 (2000).

[6] P. Ring and P. Schuck, *The Nuclear Many-Body Problem* (Springer-Verlag, New York, 1980), Chap. 13.

[7] M. Brack, C. Guet, and H.-B. Håkansson, Phys. Rep. **123**, 275 (1985).

[8] S. S. Avancini, C. C. Barros, Jr., D. P. Menezes, and C. Providência, Phys. Rev. C **82**, 025808 (2010).

[9] P. Magierski and P. H. Heenen, Phys. Rev. C **65**, 045804 (2002).

[10] D. G. Ravenhall, C. D. Bennett, and C. J. Pethick, Phys. Rev. Lett. **28**, 978 (1972).

[11] C. J. Pethick and D. G. Ravenhall, Annu. Rev. Nucl. Part. Sci. **45**, 429 (1995).

[12] J. W. Negele and D. Vautherin, Nucl. Phys. A **207**, 298 (1973).

[13] W. G. Newton and J. R. Stone, Phys. Rev. C **79**, 055801 (2009).

[14] C. J. Horowitz, M. A. Perez-Garcia, D. K. Berry, and J. Piekarewicz, Phys. Rev. C **72**, 035801 (2005).

[15] C. J. Horowitz, M. A. Perez-Garcia, and J. Piekarewicz, Phys. Rev. C **69**, 045804 (2004).

[16] C. J. Horowitz, M. A. Perez-Garcia, J. Carriere, D. K. Berry, and J. Piekarewicz, Phys. Rev. C **70**, 065806 (2004).

[17] T. Maruyama, K. Niita, K. Oyamatsu, T. Maruyama, S. Chiba, and A. Iwamoto, Phys. Rev. C **57**, 655 (1998).

[18] K. Oyamatsu, M. Hashimoto, and M. Yamada, Prog. Theor. Phys. **72**, 373 (1984).

[19] G. Watanabe, H. Sonoda, T. Maruyama, K. Sato, K. Yasuoka, and T. Ebisuzaki, Phys. Rev. Lett. **103**, 121101 (2009).

[20] K. Nakazato, K. Oyamatsu, and S. Yamada, Phys. Rev. Lett. **103**, 132501 (2009).

[21] G. Watanabe, K. Sato, K. Yasuoka, and T. Ebisuzaki, Phys. Rev. C **66**, 012801 (2002).

[22] G. Watanabe, K. Iida, and K. Sato, Nucl. Phys. A **676**, 445 (2000).

[23] H. Sonoda, G. Watanabe, K. Sato, K. Yasuoka, and T. Ebisuzaki, Phys. Rev. C **81**, 049902(E) (2010).

[24] T. Maruyama, T. Tatsumi, D. N. Voskresensky, T. Tanigawa, and S. Chiba, Phys. Rev. C **72**, 015802 (2005).

[25] O. L. Caballero, S. Postnikov, C. J. Horowitz, and M. Prakash, Phys. Rev. C **78**, 045805 (2008).

[26] D. P. Menezes, S. S. Avancini, C. Providência, and M. D. Alloy, in *Neutron Star Crust*, edited by C. A. Bertulani and J. Piekarewicz (Nova Science, Hauppauge, NY, 2012).

[27] C. J. Horowitz, Eur. Phys. J. A **30**, 303 (2006).

[28] K. Nakazato, K. Iida, and K. Oyamatsu, Phys. Rev. C **83**, 065811 (2011).

[29] H. W. Barz, J. P. Bondorf, D. Idier, and I. N. Mishustin, Phys. Lett. B **382**, 343 (1996).

[30] J. A. López and J. Randrup, Nucl. Phys. A **571**, 379 (1994); **503**, 183 (1989); **491**, 477 (1989).

[31] E. A. Uehling and G. E. Uhlenbeck, Phys. Rev. **43**, 552 (1933).

[32] A. Polanski *et al.*, Radiat. Prot. Dosim. **115**, 131 (2005).

[33] J. Taruna, Ph.D. thesis, Florida State University, AAT 3321532, 2008.

[34] A. Barrañón, C. O. Dorso, J. A. López, and J. Morales, Rev. Mex. Fís. **45**, 110 (1999).

[35] A. Vicentini, G. Jacucci, and V. R. Pandharipande, Phys. Rev. C **31**, 1783 (1985); R. J. Lenk and V. R. Pandharipande, *ibid.* **34**, 177 (1986); R. J. Lenk, T. J. Schlagel, and V. R. Pandharipande, *ibid.* **42**, 372 (1990).

[36] A. Chernomoretz, L. Gingras, Y. Larochelle, L. Beaulieu, R. Roy, C. St-Pierre, and C. O. Dorso, Phys. Rev. C **65**, 054613 (2002).

[37] A. Barrañón, C. O. Dorso, and J. A. López, Rev. Mex. Fís. **47** Suppl. 2, 93 (2001).

[38] A. Barrañón, C. O. Dorso, and J. A. López, Nucl. Phys. A **791**, 222 (2007).

[39] A. Barrañón, R. Cárdenas, C. O. Dorso, and J. A. López, Heavy Ion Phys. **17**, 41 (2003).

[40] C. O. Dorso and J. A. López, Phys. Rev. C **64**, 027602 (2001).

[41] A. Barrañón, J. Escamilla Roa, and J. A. López, Braz. J. Phys. **34-3A**, 904 (2004).

[42] A. Barrañón, J. Escamilla Roa, and J. A. López, Phys. Rev. C **69**, 014601 (2004).

[43] C. O. Dorso, C. R. Escudero, M. Ison, and J. A. López, Phys. Rev. C **73**, 044601 (2006).

[44] C. O. Dorso, P. A. Giménez Molinelli, and J. A. López, J. Phys. G **38**, 115101 (2011); Rev. Mex. Phys. **57**, S 14 (2011).

[45] G. Watanabe, K. Sato, K. Yasuoka, and T. Ebisuzaki, Phys. Rev. C **68**, 035806 (2003).

[46] C. O. Dorso, P. A. Giménez Molinelli, and J. A. López, in *Neutron Star Crust*, edited by C. A. Bertulani and J. Piekarewicz (Nova Science, Hauppauge, NY, 2012).

[47] H. C. Andersen, J. Chem. Phys. **72**, 2384 (1980).

[48] C. O. Dorso and J. Aichelin, Phys. Lett. B **345**, 197 (1995).

[49] A. Strachan and C. O. Dorso, Phys. Rev. C **55**, 775 (1997); **56**, 995 (1997).

[50] C. O. Dorso and J. Randrup, Phys. Lett. B **301**, 328 (1993).

[51] C. O. Dorso and A. Strachan, Rev. Mex. Fis. **41** Suppl. 1, 96 (1995).

[52] J. A. López and C. O. Dorso, *Lecture Notes on Phase Transformations in Nuclear Matter* (World Scientific, Hackensack, NJ, 2000).

[53] K. Michielsen and H. De Raedt, Phys. Rep. **347**, 461 (2001).

[54] C. O. Dorso, P. A. Giménez Molinelli, J. A. López, and E. Ramírez-Homs, arXiv:1208.4841.

[55] C. O. Dorso, P. A. Giménez Molinelli, J. A. López, and J. I. Nichols (private communication).

[56] Edited by K. R. Mecke and D. Stoyan, *Statistical Physics and Spatial Statistics*, Lecture Notes in Physics Vol. 554 (Springer-Verlag, Berlin, 2000), p. 111.